RESEARCH PAPER

Microstructural evolution of expansive clay during drying–wetting cycle

Tiantian Ma[1] · Changfu Wei[1,2] · Chuanqin Yao[1,3] · Panpan Yi[4]

Abstract

This paper presents a comprehensive investigation on the microstructural evolutions of expansive clay during a drying–wetting cycle, including pore size distribution (PSD) via mercury intrusion porosimetry and water distribution via nuclear magnetic resonance (NMR). The soil water characteristic curves at different soil densities and soil shrinkage curve are also obtained, and a threshold suction can be identified to distinguish the adsorptive and capillary regimes of pore water. Combined with the water distribution obtained by the NMR technique, the evolutions of the adsorptive water and capillary water during drying–wetting cycle were addressed. The measured PSD curves of the expansive soils at different suctions showed two distinct peaks, corresponding to micropores and macropores, respectively. Both variations of macropores and micropores are irreversible during the wetting–drying cycle, which partly explain the adsorptive water content decreasing when the suction is small.

1 Introduction

The behavior of expansive clayey soils, characterized by significant volume changes upon drying and wetting, can have significant implications in the safe and reliable operation of man-made infrastructure [46]. The issue is particularly relevant for routine foundation design in arid and semiarid areas [17, 45]. Upon drying–wetting process, soil microstructure (fabric/structure) changes dramatically accompanied by volume changes, which can strongly influence the soil properties, such as compressibility, shear strength and hydraulic conductivity [1, 19, 31]. Therefore, to characterize the hydro-mechanical behavior of expansive soils, it is crucial to address properly the evolution of soil microstructures during drying–wetting processes.

In studying the microstructure of soils, the pore size distribution (PSD), usually obtained from mercury intrusion porosimetry (MIP), has been proved to be an effective method [8, 30, 31].The PSD is an essential fabric element used in geotechnical engineering applications and correlated with macroscopic properties. Based on the MIP technique, some researchers have investigated the microstructural evolution of soils upon drying or wetting process [4, 5, 8, 10, 15, 17, 18, 24, 30, 33, 42, 43].

Experimental results showed that compacted expansive soils exhibit a complex structure featured with a bimodal PSD curve, showing two peaks corresponding to inter-aggregate macropores and intra-aggregate micropores, respectively. The interactions between these two structural levels are responsible for the main features of the hydro-

✉ Tiantian Ma
  ttma@whrsm.ac.cn

  Changfu Wei
  cfwei@whrsm.ac.cn

  Chuanqin Yao
  yaochuanqin@163.com

  Panpan Yi
  ppan2003@163.com

[1] State Key Laboratory of Geomechanics and Geotechnical Engineering, Institute of Rock and Soil Mechanics, Chinese Academy of Sciences, Wuhan 430071, Hubei, China

[2] College of Civil and Architectural Engineering, Guilin University of Technology, Guilin 541004, Guangxi, China

[3] University of Chinese Academy of Sciences, Beijing 100049, China

[4] Wuchang University of Technology, Wuhan 430223, Hubei, China

mechanical behavior of expansive clayey soils [19, 24, 32, 41]. Experimental results showed that mechanical loading mainly affects the inter-aggregate pores [1, 23, 30, 32], whereas hydraulic loading may affect both intra-aggregate and inter-aggregate pores [4, 23, 35]. During drying, the reduction of macropores can be accompanied by an increase in micropores [4, 7, 14, 35], and the trend upon wetting is reversed [17, 34]. However, the microstructural evolution of expansive soils upon drying and wetting is a complex issue due to the multi-scale interactions between inter-aggregate pores and intra-aggregate pores, influenced by soil type, clay minerals, and clay content. The evolution of soil structure upon mechanical or hydraulic loading and the data obtained by microstructural analyses techniques require significant interpretative work [17].

Other than the PSD, one of the most important elements of soil microstructure is the water distribution in the pores, strongly controlling over the mechanical and seepage behavior of partially saturated soils. The behavior of unsaturated soils is complicated by the presence of both air and water that also affects the evolution of pore network and water distribution. Unlike the PSD, the water distribution is uneasy to be quantitatively investigated. Few studies have involved the evolution of water distribution during drying–wetting cycle, which is still not well understood.

The development of nuclear magnetic resonance (NMR) technique provides an innovative method to investigate the water distribution of soils and mobility in porous media [6]. NMR T_2 (spin–spin relaxation) measurements are highly sensitive to the presence of water in soils, and the obtained proton spin–spin relaxation time (T_2) distribution reflects the structural arrangements of surrounding water molecules, and thus the surrounding soil structure to some extent. NMR is a reliable method for distinguishing the capillarity-dominated water and the adsorption-dominated water, since they are subjected to forces of different origins [13, 26, 37].

In this paper, drying–wetting cycle tests were conducted on an expansive soil using the humidity control technique, by which the soil–water characteristic curves (SWCCs) and soil shrinkage curve (SSC) were determined. Then comprehensive analyses of the soil microstructure were performed through MIP and NMR techniques that allowed tracking the microfabric evolution, including PSD and the water distribution, during drying–wetting cycle.

2 Materials and methods

An expansive clay from Ningming, Guangxi, China, was used in the drying–wetting tests. Table 1 shows the chemical and physical properties of the soil. The

mineralogical composition was determined by X-ray diffraction analysis, and the specific surface area of clay sample was gravimetrically measured using ethylene glycol mono-ethyl ether (EGME) retention procedure for four duplicate samples and only the mean value is reported here. The grain size distributions of the expansive are shown in Fig. 1. The average free expansion ratio is 370%, implying that the soil is strong expansive soil.

The materials were first air-dried, pulverized and sieved though a 0.5-mm sieve for use in the present experimental study. The passing particles were mixed with distilled water to reach a chosen gravimetric water content of 15%. The moist sample was sealed in a plastic bag for more than 48 h in order to achieve a homogeneous water distribution. After that, the moist sample was compacted statically to a targeted dry density of 1.2 g/cm^3 into a Teflon cylinder 45 mm in diameter and 20 mm in height. The sample preparation in the NMR measurement is the same with the drying–wetting tests. Instead of using conventional steel odometer rings, special Teflon plastic rings were used to eliminate the influence of Fe in the magnetic field (NMR measurement). All the samples were saturated, based on the vacuum method, in a sealed chamber with distilled deionized water for 4 h, and then remained immersed in the distilled water for another 24 h to ensure full saturation. For distinguishing adsorptive water and capillary water, the SWCCs of soil powders were also measured. For the drying branch, the initial water content of soil powders is 30%, where the passing particles were mixed with distilled water to reach the chosen gravimetric water content.

2.1 Drying–wetting experiments

The drying–wetting tests were conducted using the humidity control techniques, and the SWCCs at different densities were obtained for various hydraulic paths [22]. The saturated salt solutions were maintained in closed chambers to control relative humidity, and Table 2 summarizes the humidity and suction values for the selected series of saturated salt solutions at the temperature of 27 °C [22]. The relationship between total soil suction and relative humidity (RH) is described by Kelvin's equation, i.e.,

$$s_t = -\frac{R \cdot T}{V_w} \ln RH \tag{1}$$

where s_t is the total soil suction (kPa); R is the universal gas constant (8.314 J/mol·K); T is absolute temperature (K); V_w is specific molecular volume of water (m^3/kmol), RH is the relative humidity. Humidity-controlled techniques are applicable in the range of relatively high total suction, generally greater than about 4 MPa.

As illustrated in Fig. 2a, two identical saturated specimens were placed in each sealed chamber containing a

Table 1 Chemical and physical properties of the expansive soil

Mineralogical components	Concentration (weight/weight) (%)	Properties	Unit	Magnitude
Quartz	27.92	CEC[a]	meq/100 g	26
Illite	21.57	Specific surface area	m^2/g	484
Montmorillonite	11.31	Specific gravity	–	2.85
Albite	39.21	Liquid limit	%	218
		Plastic limit	%	58
		Plasticity index	–	160
		Initial air-dried water content	%	8

[a]Cation exchange capacity
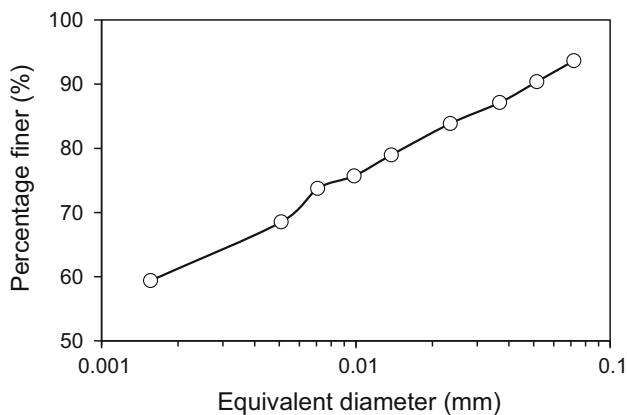
Fig. 1 Particle size distribution data for expansive clay

specific saturated salt solution corresponding to some desired level of relative humidity for drying. Twelve samples were put into the chamber with saturated LiBr solution (the lowest RH) for wetting test. In the relative humidity testing, the soil sample is adsorbed or released water via water vapor. The water content corresponding to each suction is obtained by weighing the soil sample after equilibrium. Specimens were weighed regularly until the total mass remained constant for 2 weeks. When the equilibrium state was reached, the sample was weighed, and the corresponding water content was determined. The time needed for the soil mass to reach equilibrium was about 2 months for each RH. After that, the samples dried in the LiBr solution (about 382 MPa) were put into the other 10 saturated salt solutions separately for wetting test. The experimental procedure was the same as that of drying process and the time for equilibrium was also about 2 months. All tests were conducted in the laboratory with an ambient temperature controlled at 27 ± 1 °C. For distinguishing adsorptive water and capillary water, the soil powders were also placed into the chamber to obtain SWCCs during drying–wetting cycle using the same procedure.

For the soil shrinkage curve, the suction was also controlled by humidity control techniques and the volume deformation was obtained by the digital camera. After fully saturation, the sample was carefully extruded out of the cylinder mold and was transferred onto the sample holder, as illustrated in Fig. 2b. A thin grease film was spread on the surface of the holder to reduce the friction between the sample and plate. The purpose of such treatment was to remove any constraint on the boundary of the soil sample, so that soil can freely deform under various environmental loadings of drying [12]. The specimen with holder was placed on a digital balance to monitor the weight change during drying. A digital camera was fixed on a holding arm steadily and center-aligned with the center positions of the specimen. During drying process, the still digital camera took images of the soil specimen for subsequent image

Table 2 Saturated salt solution and corresponding suction at 27 °C

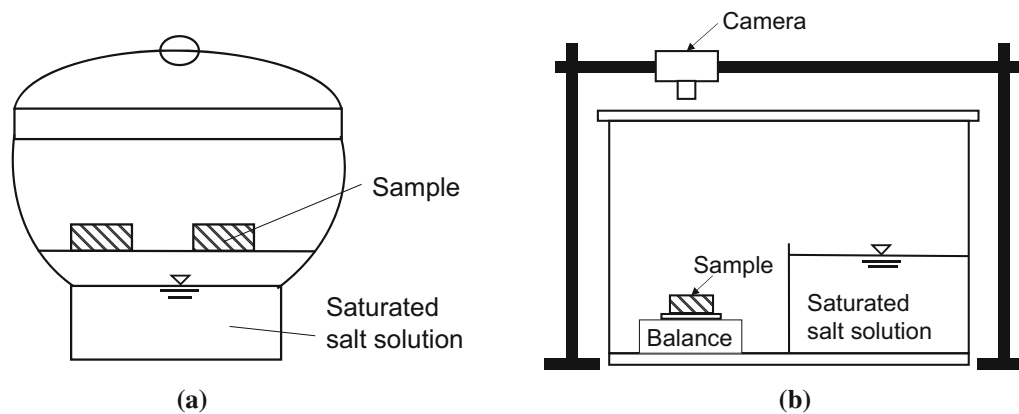| Saturated salt solution	RH (%)	Suction (MPa)	Saturated salt solution	RH (%)	Suction (MPa)
$CuSO_4 \cdot 5H_2O$	97.1	4.08	NaCl	75.2	39.50
K_2SO_4	96.9	4.36	$K_2CO_3 \cdot 2H_2O$	43.2	116.36
KNO_3	93.1	9.95	$MgCl_2 \cdot 6H_2O$	32.6	155.20
$ZnSO_4 \cdot 7H_2O$	90.0	14.61	LiCl	11.3	302.38
KCl	84.0	24.08	LiBr	6.4	382.18
$(NH_4)_2SO_4$	80.7	29.65			

Fig. 2 Sketches of vapor equilibrium method for SWCC and SSCC

processing to determine the total volume deformation. In the calibration tests, it was found that the sample shrank isotropically, and the radical and vertical deformations are almost the same. Therefore, only radical deformation is monitored in the subsequent tests. The accuracy of the measured radical deformation depends on the pixels of the images and the width of the field of view. The images analyzed in this paper were captured using a Nikon D5600 digital still camera, which has an image resolution of 2587×2499 pixels. The diameter and height of the sample are 45 mm and 20 cm, respectively. The digital image processing technique can achieve an accuracy in the measurement of radical deformation of 0.4×10^{-3}. The ImageJ software was used to determine the radical displacement. Because the diameter of the sample is proportional to the pixels of the image, the change of pixels in the images can be used to calculate the radical deformation [11, 20]. The digital balance reads the weight change throughout the test, and therefore the degree of saturation or water content of soil specimen can be calculated. When the specimen weight did not change, the next relative humidity was applied. During drying process, the relative humidity was decreased slowly to prevent inhomogeneous moisture distribution and to avoid crack development.

2.2 Microstructural investigation

The evolution of PSD for the soil specimens upon drying–wetting cycle was investigated using the MIP technique (ASTM D4404–18). The principle of MIP test is based on the Laplace–Young law, relating capillary pressure p_c to capillary radius r for pores of cylindrical shape [31],

$$p_c = \frac{-2\gamma\cos\theta}{r} \qquad (2)$$

where γ is the mercury surface tension (0.484 N/m at 25 °C [11]). θ is the contact angle between the liquid mercury and the solid surface (140° [11]). During the test, pressure is

increased stepwise and the intruded volume of mercury at each step is measured simultaneously.

The MIP analysis requires a pre-treatment of specimens to remove the pore water with minimal impact on the soil structure. This was achieved by the so-called freeze-drying technique [10]. The samples after SWCC determination were immersed into liquid nitrogen (− 190 °C). Under these conditions, water with a cryptocrystalline structure and volumetric expansion is largely eliminated [10]. Then, the frozen samples were placed in a vacuum chamber of a freeze-dryer to sublimate the amorphous ice under vacuum condition and − 60 °C for 48 h. After treatment, the specimens were sealed in airtight plastic containers and stored in a desiccator prior to MIP analysis.

The water distribution in soil specimens upon drying–wetting cycle was investigated using the NMR technique. The NMR T_2 relaxation measurements were taken using a CPMG (Carr–Purcell–Meiboom–Gill) pulse sequence. A proton (e.g., H^+) bears a spin magnetic moment. If a magnetic pulse of a radio frequency is applied, the magnetization can be temporarily oriented to a new, unstable direction. Once the pulse is removed, each proton spin emits the absorbed energy and returns to the initial equilibrium position through a series of relaxation processes, which can be characterized using NMR. During the relaxation process, the NMR signal intensity suffers from attenuation freely, monitored by the Carr–Purcell–Meiboom–Gill (CPMG) pulse sequence. The relaxation process can be described by [37]

$$M(t) = M_0 \exp\left(\frac{-t}{T_2}\right) \qquad (3)$$

where t is time, $M(t)$ is the magnetization at time t, M_0 is initial magnetization, and T_2 is the transverse relaxation time.

Measuring the decay of echo amplitudes M during the sequence can track the transverse magnetization relaxation. The shape of CPMG curve is related to the transverse

relaxation time T_2 of pore water in porous media. Through Fourier transformation, the T_2 distribution of pore water can be obtained by the inversion of the relaxation decay curve. For water-saturated spherical pores, T_2 is proportional to their characteristic radius, r. The relationship between T_2 and r can be written as

$$\frac{1}{T_2} \approx \rho_2 \frac{f}{r} \tag{4}$$

where ρ_2 is the surface relaxivity of pore walls in porous media, which is related to the physicochemical properties of the soil particle surface. f is a shape factor that assumes a value of 1, 2 or 3 for planar, cylindrical or spherical pores, respectively. T_2 is proportional to the pore radius, which means that the smaller the pore, the smaller the value of T_2, that is, the adsorptive water or the water in the smaller pores relaxes faster than the free water or the capillary water in larger pores. The area under T_2 distribution curve represents the water mass corresponding to the T_2 range [37]. Therefore, T_2 distribution curve can represent the water distribution of the soil. After the samples equilibrated at the given relative humidity, the samples were put into NMR sample tube one by one to isolate them from the environment. Put the sample tube with the sample into the NMR apparatus, and the measurement of NMR signal intensity is controlled by software.

3 Results and discussion

3.1 Soil water characteristic curves (SWCCs) and soil shrinkage curve (SSC)

Figure 3 summarizes the soil–water characteristic curves of expansive soil upon drying–wetting cycle determined by the humidity-controlled method, where the gravimetric water content is adopted as x-coordinate. Gravimetric water content is a basic physical variable, which is independent on the volume of soil sample. The volumetric deformation has no influence on the gravimetric water content. The solid lines in Fig. 3 depict the SWCCs for the compacted sample with dry density of 1.2 g/cm³ and the dashed lines for the powder sample. It is clear that SWCCs for different compactness are characterized by hysteresis during the drying–wetting cycle. The hysteresis diminishes with the increase in suction and disappears when the suction increases to about 300 MPa, where the corresponding water content is only 0.06.

In general, water phase in unsaturated porous media is retained by both capillary and adsorptive forces [16, 39, 40]. Accordingly, SWCC can be decomposed into capillary and adsorptive regimes. Capillarity prevails at low suction due to surface tension on a curved air–water
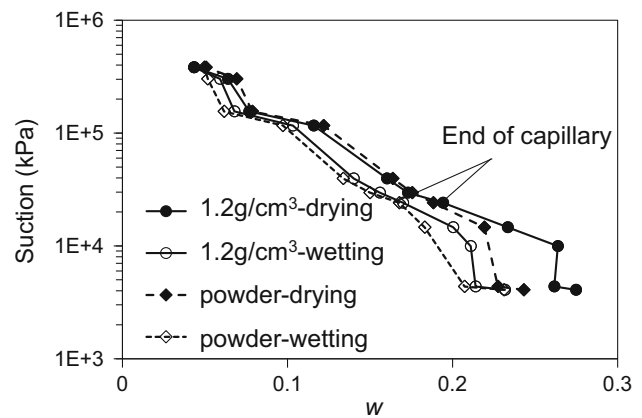

Fig. 3 Soil-water characteristic curves for drying and wetting

interface in soil pores, whereas adsorption prevails at high suction referring to all the interfacial forces involved in adsorbing the water films onto the grain surfaces due to the presence of exchangeable cation hydration, mineral surface, or crystal interlayer surface hydration [21]. As governed by Kelvin's equation, the SWCC within the capillary regime strongly depends on the compactness, while the adsorption is only controlled by the type and quantity of minerals, and practically independent of compactness.

In Fig. 3, the drying and wetting branches of the soil powder are generally located below those of the compacted sample at the low suction range, attributing to the difference in the pore structure and density of the soil. With the increase in suction, SWCCs of the compacted sample and soil powder tend to merge into the same curve beyond a certain suction of 24 MPa. That is, the structural effects are only visible at the low suction range (in the regime of capillary) and tend to vanish at the air-drying end (in the regime of adsorption). Therefore, for the tested expansive soil, one can define the threshold suction of 24 MPa as the end of capillarity (Fig. 3), which can be used to distinguish the capillary and adsorption regimes. These findings are consistent with the experimental results in Ref. [17], where the intact SWCC and reconstituted SWCC tend to merge into a single curve beyond a certain suction for all clays. Similar results have also been obtained on clay samples with different void ratios under constant-volume conditions [32]. Consider the compacted expansive soils, exhibiting a bimodal pore structure as will be seen in the subsequent PSD experiments. In these soils, the pore water can be divided into the water in the inter-aggregate voids (macrostructural water) and the water in the intra-aggregate pores (microstructural water) [9]. It is assumed that the pore water beyond suction of 24 MPa is primarily adsorbed into the micropores, where capillary water in the macropores was almost absent [32]. In the regime of adsorption, the compactness does not affect the water state in the

micropores. As the suction is lower than 24 MPa (i.e., in the capillary regime), the effect of compactness comes into play and can significantly influence both the drying than wetting branches of the SWCCs.

3.2 Water distribution

Soil deformation under drying can be quantified as the void ratio variation with suction. The volume deformation during drying process was calculated by the variation of pixels in the photograph shot by camera considering the volume of saturated sample as the reference state. In the calculation, the isotropic deformation is assumed and the vertical deformation equals to the radical deformation. The measured soil shrinkage curve is shown in Fig. 4, and the cut-off point of the capillary and adsorption regimes is marked as solid circle. The shrinkage curve of the compacted expansive soil is S-shaped sigmoidal curve consisting of three stages: normal shrinkage, residual shrinkage and zero shrinkage. By analyzing on mechanism, the SSC can be conceptualized in two regimes distinguished by capillary and adsorption SWR mechanisms [20]. During drying process, most of the shrinkage deformation occurred in the capillary regime and the interfacial surface tension tightens the skeleton through the capillary force. With continued drying, the capillary water starts to diminish, and the SSC becomes gradually smooth with the slope begins to change. Meanwhile, the adsorptive effect onsets and the shrinkage is dominated by the adsorptive forces stemming from the physicochemical interaction among soil particles and water film, including electrostatic forces, van der Waals attraction, and so on. Because the hydrated water on the particle surfaces is mostly away from particle contacts, their mechanical effect on shrinkage is less effective than in the capillary regime [20]. As soil water further decreases, the SSC gradually flattens out and the total volume of sample has been considered unchanged with the removal of the
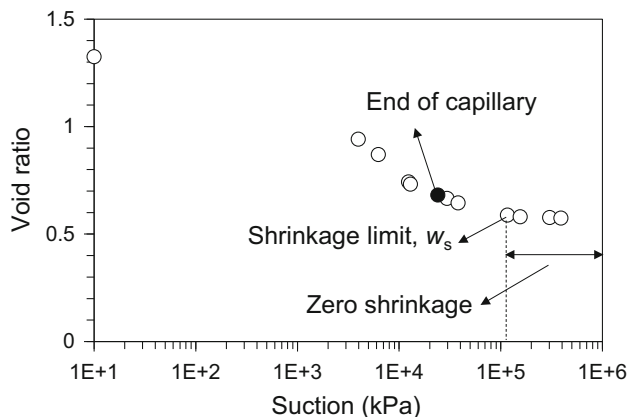
tightly adsorptive water. In the zero shrinkage state, the shrinkage of pores has been considered to compensate for the internal micro-fissures developed in the boundary at the interface between clay and silt grains [36], leading to much less pronounced shrinkage behavior of the total volume.

Figure 5 depicts the distribution curves of T_2 determined by the NMR technique of the soil samples with different water contents during the drying–wetting cycle. The magnitude of T_2 (the x-axis) represents the pore radius of soil, while the NMR signal intensity (the y-axis) accounts for the water content in the pores. It can be seen that T_2 spans several orders of magnitude and centers around 0.05–5 ms. The area under the T_2 distribution curve is termed as the "peak area," which represents the population of water molecules, indicating the amount of water content in the soil sample. In Fig. 6, the peak area and water content of the sample shows a good linear relationship during the hydraulic cycle, showing that the NMR signal is capable of capturing the amount of water molecules in the soil sample [37]. When the water content is very low, the experimental data deviate from the linear relation, probably due to the strong interaction between the water film and particle surface.

From Fig. 5a, one can see that with the increase in suction, the NMR signal corresponding to the larger T_2 decreases gradually, clearly indicating that the pore water drainage occurs sequentially from larger pores to smaller pores. This result is consistent with what expected theoretically, since the capillary effect of the pore water in larger pores is weaker than that in smaller pores. Figure 5a illustrates that when the soil becomes unsaturated, the T_2 distribution curve shifts leftward so that in the range of smaller T_2 content, the measured NMR signal is much larger than that of saturated soil. This occurs probably due to the double-level structure of compacted expansive soil. The sample undergoes a large shrinkage when the suction of 4 MPa is applied during drying process. The macroscopic pore shrinks very apparently, accompanied by the growth and aggregation of soil particles leading to an increase in the amount of microscopic pores [29]. This phenomenon can be demonstrated by PSD curve. With further drying, the rate of NMR signal attenuation decreases slowly corresponding to the gradual decrease in the water content. During this process, the NMR signal of larger T_2 disappears gradually, and the measured NMR signal in the range of smaller T_2 increases slightly, indicating that the shrinkage rate decreases. This is consistent with the PSD curves obtained by MIP upon drying process.

Figure 5b depicts the evolution of T_2 distribution upon wetting process, where the T_2 distribution of saturated sample is chosen as a reference curve. With the decrease in suction, the T_2 distribution tends to be wider and the value of T_2 is increasing gradually. That is, water begins to enter
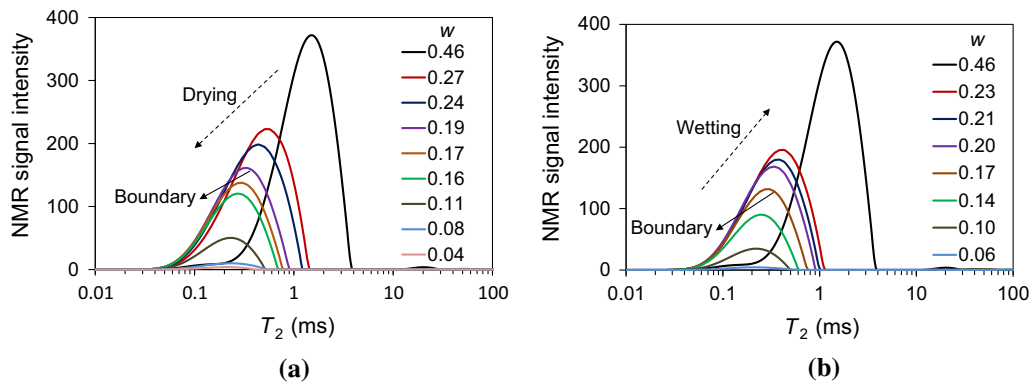

Fig. 4 Change of void ratio with suction during drying

Fig. 5 The proton spin–spin relaxation time, T_2, distribution curves: **a** drying; **b** wetting
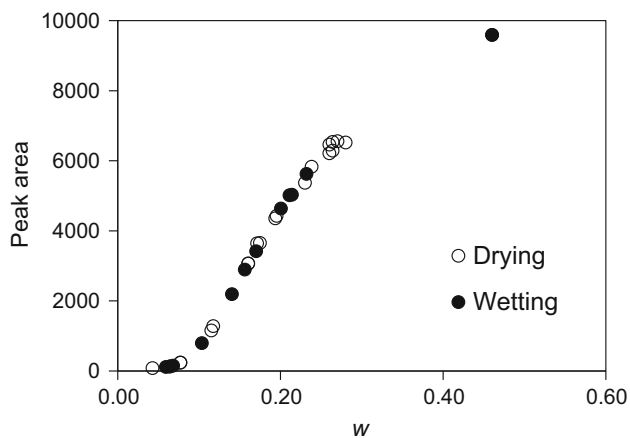

Fig. 6 Relationship between the water content and NMR signal intensity

the microscopic pore and then macroscopic pore during wetting process. Unlike drying process, in the small range of T_2 (the left side of Fig. 5b), the T_2 distribution of sample with low water content is always below that of high water content, i.e., the water distributions during drying–wetting processes are not consistent. This occurs probably due to the adsorptive hysteresis effect.

Due to the significant physicochemical interactions between the grain surfaces and pore water, the adsorptive water relaxes faster than the capillary water, and the measured value of T_2 is smaller [2, 3, 38]. Therefore, the left part of T_2 distribution is associated with the adsorbed pore water, whereas the right part is related to the capillary pore water. As mentioned above, the suction of 24 MPa is considered as the threshold point distinguishing the adsorption and capillary regimes. Combined with the T_2 distributions obtained by NMR, one can define the curve with the water content of 0.19 (at the suction of 24 MPa) as the boundary for adsorptive water distribution without capillary water upon drying process and the T_2 curve with the water content of 0.17 (at the suction of 24 MPa) is defined as the boundary for adsorptive water distribution

upon wetting process. The boundary curve inside represents the adsorptive water while the outside represents the capillary water. The largest T_2 of adsorptive water is 0.86 ms, which is consistent with the conclusion in Ref. [14] about the range of T_2 for the adsorptive water in frozen soils is 0.9–1.1 ms.

In the regime of adsorption, capillarity is negligible, and all the soil water is adsorbed. In the capillary regime, both adsorbed water and capillary water are present in the soil pores. Therefore, the T_2 distribution curve in the capillary regime minus the boundary T_2 distribution for the adsorptive water is the capillary water distribution. Figures 7 and 8 depict the distributions of adsorptive and capillary water at different water contents upon drying–wetting cycle. From Figs. 7 and 8, there is a small plateau region at low T_2 time in the T_2 distribution curve at full saturation (with water content of 0.46), which appears to be coincident with the T_2 distribution curve for the water content of 0.08. This part of water is always there, keeping unchanged during the drying–wetting cycle, and even the same as that in the powder sample. This part of water may be the strongly bound water, only existing in the stern layer of diffuse electric double layer.

Figure 9 depicts the water distributions of compacted sample and power sample at suction of 24 MPa. It can be observed that the T_2 distributions of water in samples with different compactness are almost coincident. This further proves the independence of the adsorptive water distribution on the soil structure, consistent with the results of SWCCs. This also provides some evidence that the compactness has negligible impact on the microstructure.

Based on the T_2 distributions of adsorption and capillary regimes, with the total water content, one can calculate the adsorptive water content (and thus the capillary water content). Let A_a and A_c be the peak areas for the adsorptive and capillary water, respectively. Then the adsorptive and capillary water contents are given by
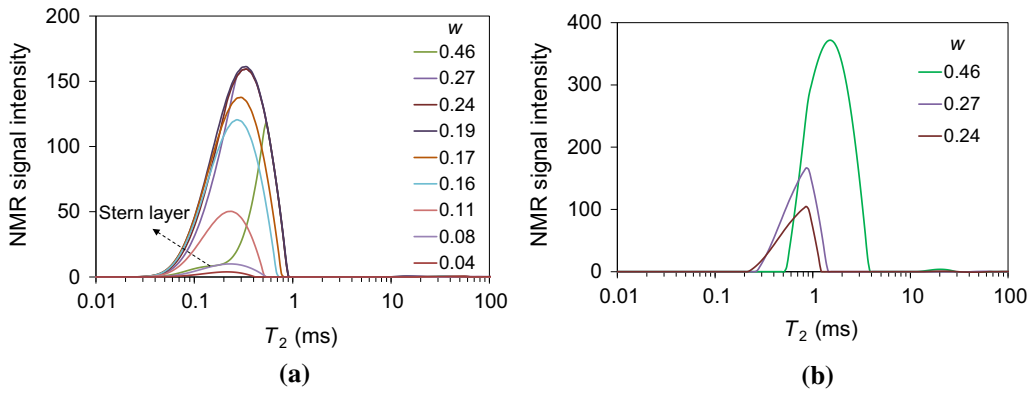
Fig. 7 The proton spin–spin relaxation time, T_2, distribution curves during the drying process: **a** adsorptive water; **b** capillary water
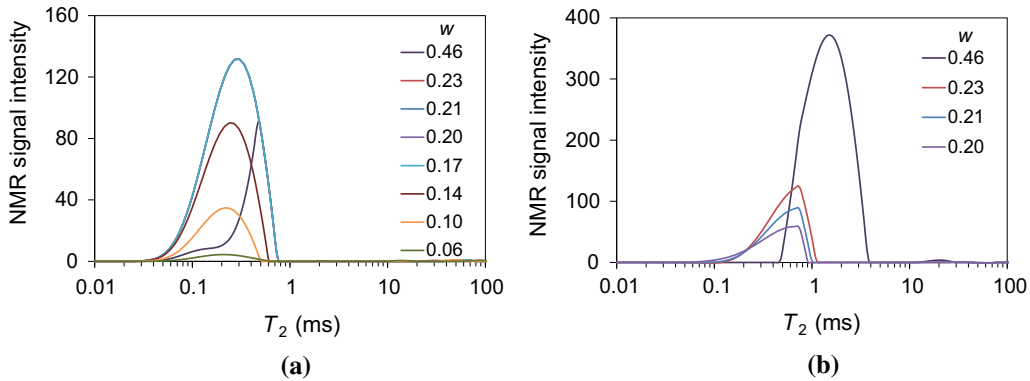

Fig. 8 The proton spin–spin relaxation time, T_2, distribution curves during the wetting process: **a** adsorptive water; **b** capillary water
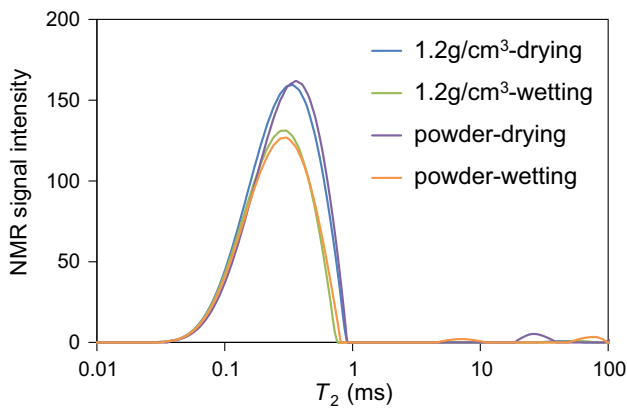

Fig. 9 The proton spin–spin relaxation time, T_2, distribution curves of adsorptive water of samples with different densities

$$w_a = \frac{w}{A_t} \cdot A_a; \quad w_c = \frac{w}{A_t} \cdot A_c \tag{5}$$

where w_a and w_c are the adsorptive and capillary water contents, respectively. A_t is the total peak area for the corresponding water content.

Figure 10 depicts the variations of adsorptive water content and capillary water content with suction for the expansive soil during drying–wetting cycle. In the adsorption regime, the capillary water is absent and the adsorptive water is solely responsible for the change in soil water. The hysteresis of the adsorptive water content is unexpectedly significant. Because capillary and adsorption water retention mechanisms are different in physics, the soil water retention hysteretic mechanisms should be different too. For capillarity, the hysteresis is often attributed
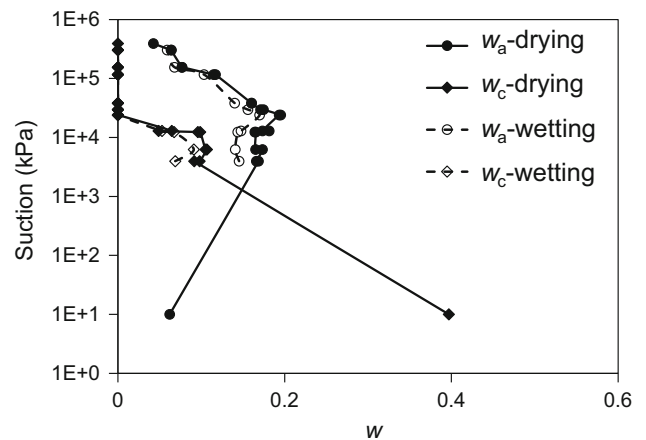

Fig. 10 The variations of adsorptive and capillary water contents with the suction

to the differences in solid–liquid-air contact angle and pore geometries. For adsorption, the hysteresis has primarily been attributed to different and yet coexisting hydration mechanisms [21]. As the suction decreases less than 24 MPa (when the capillary effect comes into play), the adsorptive water content starts to decrease, in contrast to the common sense that the maximum adsorptive water content is constant. This is due to the specific variation of pore structure for the certain expansive soil. The phenomenon of growth and aggregation of soil particles has also been observed during the drying process, in which the micropores and the corresponding adsorptive water content increase. The phenomenon of growth and aggregation of soil particles has also been observed during the drying process, in which the micropores and the corresponding adsorptive water content increase. Most of the shrinkage upon drying occurs as the relative humidity reduces from 100 to 97%, in which the microspores increases dramatically and the corresponding adsorptive water content increases. Therefore, the adsorptive water content at relative humidity of 97% is larger than the bottom point of the w_a-drying curve.

3.3 Pore size distribution

Figure 11 depicts the evolution of PSD with water content along drying–wetting cycle using the MIP technique. The PSD curve of saturated sample ($w = 0.46$) shows a typical bimodal pattern (characterized by the presence of macropores and micropores), consistent with the results of compacted expansive soils [4]. The diameters of macropore (inter-aggregate pores) and micropore (intra-aggregate pores) are about 6 μm and 12 nm, respectively. Based on the Laplace–Young equation, the pore diameter corresponding to the threshold suction for distinguishing the capillary and adsorption regimes, 24 MPa, is 12 nm, which is of the same order as the diameter of micropore.

Therefore, the micropores are deemed to be mainly associated with the water retention dominated by adsorption mechanism [27, 28]. The dual-pore structural arrangement of the sample is qualitatively confirmed by the SEM images of the saturated sample shown in Fig. 12. Large macropores are evident in Fig. 12(a), and the average inter-grain pore size between 5 and 10 μm is detected, in agreement with PSD measurements (Fig. 11). At larger magnification, the lamellar structure can be seen in Fig. 12b, showing the micropores in the clay aggregates.

When the soil enters into unsaturated state upon drying, macropores reduce significantly, being compensated by an increase in microporosity, whereas the pore entrance diameters corresponding to the two peaks remain unchanged. Such an increase in microporosity has been observed in other studies and can be explained by the particle aggregation, in which some macropores are transformed into the micropores [15]. Our results show that most of the shrinkage upon drying occurs as the relative humidity reduces from 100 to 97%. The variation of PSD can explain the change of water distribution obtained by the NMR technique, where the water content with smaller T_2 increases significantly due to the increase in micropore volume going beyond that part of saturated sample. With drying further, the macropore volume reduces gradually down to a point where the pore is dominated by micropore and the proportion of macropore is relatively small. The evolution of the PSD upon wetting was also investigated, shown in Fig. 11b, where the PSD of saturated sample is chosen as a reference. As expected, the PSD change trend of the soils is reversed and rewetting the soil shows an increase in the macroporosity with the decrease in the microporosity.

The evolution of microstructure has been investigated further by computing the void ratios associated with microporosity (e_m) and macroporosity (e_M). This requires the definition of a boundary between micro and macro and
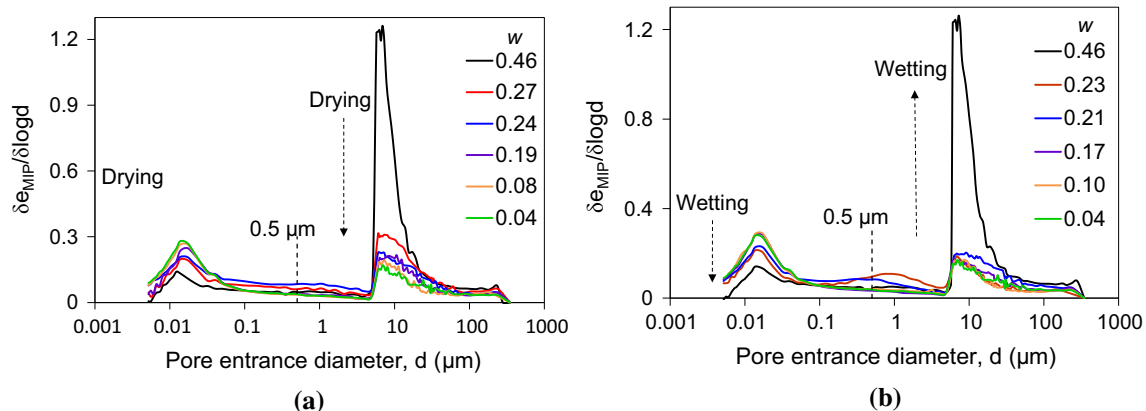

Fig. 11 Pore size distributions: a drying process; b wetting process

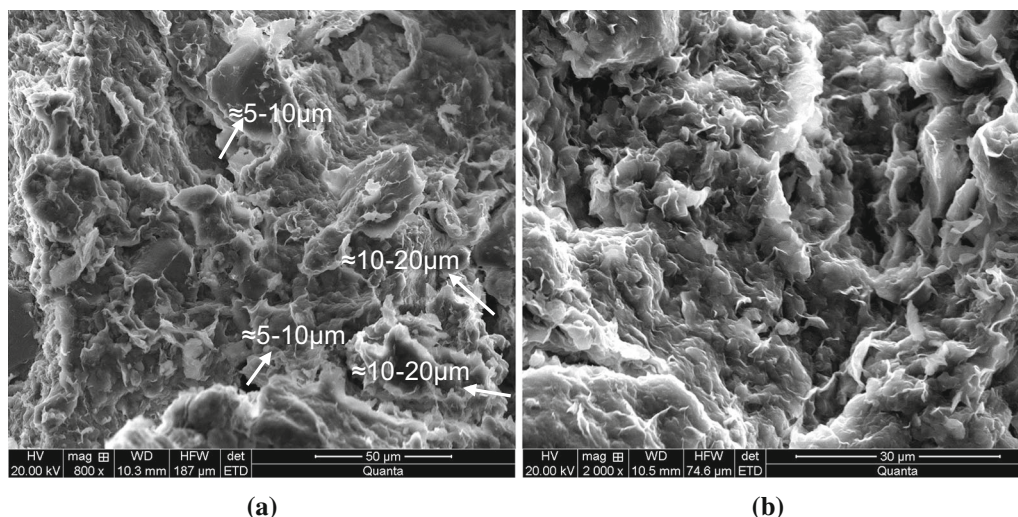**Fig. 12** Scanning electron microscope images of expensive soil at full saturation: **a** × 800 magnification; **b** × 2000 magnification

different criteria have been proposed to separate the two scales [10, 17, 25, 32]. In the above experimental results, the PSD does not shift upon drying–wetting cycle, and the macropore and micropore peak diameters are unchanged. Hence, the valley of PSD curve can be accepted as the value that separates the inter-aggregate and the intra-aggregate pore spaces, where the diameter corresponding to valley is about $0.1 \sim 4$ μm. The average diameter of 0.5 μm is adopted as the threshold value, similar to the boundary obtained in Ref. [17]. Because the porosity in this section is very small, the change of the threshold value in this section will cause insignificant effect on the results.

Figure 13 presents the evolution of e_m and e_M along the drying–wetting path, where the y-axis represents the proportion of e_m and e_M in the total e. It is noted that the MIP provides information about the diameter of the entrance pore size (not the actual pore size) [17]. In addition, the void ratio, e, is generally underestimated by MIP [42], due to undetected porosities [31, 44]. Therefore, the proportion of e_m and e_M in the total e is adopted here to illustrate the variation trends of macropores and micropores. Figure 13 shows two distinct domains, with the macropores dominated in the low suction while the micropores dominated in the high suction. The boundary suction between these two domains is about 15 MPa, close to the suction value distinguishing the adsorption and capillary regimes reflected on the retention curves. With the suction increasing further, the shrinkage rate decreases. When the suction rises beyond 120 MPa (RH = 43%), the soil enters a phase of residual shrinkage with vanishing volume change. For the subsequent wetting process, the evolution of macropores and micropores is almost reversible in the high suction range, about 15–380 MPa. With the decrease in suction, the change of pore structure becomes irreversible,
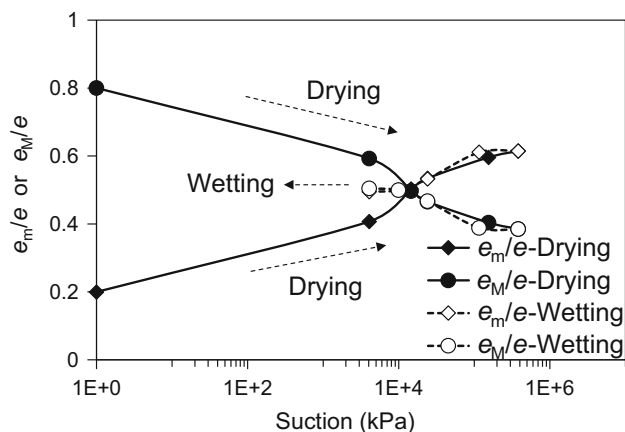

Fig. 13 Development of macropores and micropores with the suction during drying–wetting cycle

including the micro-pores. This is inconsistent with the observations in the previous references [17, 32], where it was suggested that the evolution of micropores was reversible.

4 Conclusions

A series of experimental investigations were conducted on the retention and microstructure behavior of expansive soil upon drying–wetting cycle. The soil water characteristic curves of samples at different densities and the soil shrinkage curve were measured by the humidity control technique. The microfabric evolution for pores and the water distributions of samples were obtained by MIP and NMR techniques, respectively. Based on the experimental results, the threshold suction of 24 MPa is defined for distinguishing adsorption and capillary regimes for the

expansive soil. Correspondingly, the soil shrinkage curve can be divided into two states and each is governed by two mechanisms: capillary and adsorption. Combined with the NMR technique, a boundary adsorptive water distribution curve is defined at the suction of 24 MPa, inside which represents the adsorptive water and outside which represents capillary water. Based on the method, the adsorptive and capillary water distributions were obtained, and the variations of adsorptive and capillary water contents with the suction upon drying–wetting cycle were determined. The measured pore size distribution curves showed two distinct peaks corresponding to the micropores and macropores for saturated expansive soil. Upon drying process, the PSD curve progressively evolved and the microporosity was found to be dominant for higher suction. Using the valley as a reference state to determine the boundary between micro and macro, the evolution of microporosity and macroporosity with suction has been investigated. It was observed that the microporosity also has permanent deformation upon drying and wetting cycle.

References

1. Al-Mukhtar M, Belanteur N, Tessier D, Vanapalli SK (1996) The fabric of a clay soil under controlled mechanical and hydraulic stress states. Appl Clay Sci 11(2–4):99–115. https://doi.org/10.1016/S0169-1317(96)00023-3

2. Bayer JV, Jaeger F, Schaumann GE (2010) Proton nuclear magnetic resonance (NMR) relaxometry in soil science applications. Open Magn Reson J 3:15–26. https://doi.org/10.2174/1874769801003010015

3. Bird NRA, Preston AR, Randall EW, Whalley WR, Whitmore AP (2005) Measurement of the size distribution of water-filled pores at different matric potentials by stray field nuclear magnetic resonance. Eur J Soil Sci 56:135–143. https://doi.org/10.1111/j.1351-0754.2004.00658.x

4. Burton GJ, Pineda JA, Sheng DC, Airey D (2015) Microstructural changes of an undisturbed, reconstituted and compacted high plasticity clay subjected to wetting and drying. Eng Geol 193:363–373. https://doi.org/10.1016/j.enggeo.2015.05.010

5. Casini F, Vaunat J, Romero E, Desideri A (2012) Consequences on water retention properties of double-porosity features in a compacted silt. Acta Geotech 7(2):139–150. https://doi.org/10.1007/s11440-012-0159-6

6. Cheng K, Heidari Z (2017) Combined interpretation of NMR and TGA measurements to quantify the impact of relative humidity on hydration of clay minerals. Appl Clay Sci 143:362–371. https://doi.org/10.1016/j.clay.2017.04.006

7. Cuisinier O, Laloui L (2004) Fabric evolution during hydromechanical loading of a compacted silt. Int J Numer Anal Methods Geomech 28(6):483–499. https://doi.org/10.1002/nag.348

8. Delage P, Audiguier M, Cui YJ, Howat MD (1996) Microstructure of a compacted silt. Can Geotech J 33(1):150–158. https://doi.org/10.1139/t96-030

9. Delage P, Marcial D, Cui YJ, Ruiz X (2006) Ageing effects in a compacted bentonite: a microstructure approach. Géotechnique 56(5):291–304. https://doi.org/10.1680/geot.2006.56.5.291

10. Diamond S (1970) Pore size distributions in clays. Clay Clay Miner 18(1):7–23. https://doi.org/10.1346/CCMN.1970.0180103

11. Dong Y, Lu N (2017) Measurement of suction-stress characteristic curve under drying and wetting conditions. Geotech Test J 40(1):107–121. https://doi.org/10.1520/GTJ20160058

12. Fleury M, Kohler E, Norrant F, Gautier S, M'Hamdi J, Barré L (2013) Characterization and quantification of water in smectites with low-field NMR. J Phys Chem C 117(9):4551–4560. https://doi.org/10.1021/jp311006q

13. Jaeger F, Shchegolikhina A, van As H, Schaumann G (2010) Proton NMR relaxometry as a useful tool to evaluate swelling processes in peat soils. Open Magn Reson J 3:27–45. https://doi.org/10.2174/1874769801003010027

14. Koliji A, Laloui L, Cusinier O, Vulliet L (2006) Suction induced effects on the fabric of a structured soil. Transport Porous Med 64(2):261–278. https://doi.org/10.1007/s11242-005-3656-3

15. la Morena GD, Asensio L, Navarro V (2018) Intra-aggregate water content and void ratio model for MX-80 bentonites. Eng Geol 246:131–138. https://doi.org/10.1016/j.enggeo.2018.09.028

16. Lebeau M, Konrad JM (2010) A new capillary and thin film flow model for predicting the hydraulic conductivity of unsaturated porous media. Water Resour Res 46:W12554. https://doi.org/10.1029/2010WR009092

17. Liu XF, Buzzi O, Yuan SY, Mendes J, Fityus S (2016) Multi-scale characterization of retention and shrinkage behaviour of four Australian clayey soils. Can Geotech J 53(5):854–870. https://doi.org/10.1139/cgj-2015-0145

18. Liu XF, de Carteret R, Buzzi OP, Fityus SG (2016) Microstructural effects of environmental salinity on unbound granular road pavement material upon drying. Acta Geotech 11(2):445–451. https://doi.org/10.1007/s11440-015-0393-9

19. Lloret A, Villar MV (2007) Advances on the knowledge of the thermo-hydro-mechanical behaviour of heavily compacted "FEBEX" bentonite. Phys Chem Earth 32(8–14):701–715. https://doi.org/10.1016/j.pce.2006.03.002

20. Lu N, Dong Y (2017) Correlation between soil-shrinkage curve and water-retention characteristics. J Geotech Geoenviron 143(9):04017054. https://doi.org/10.1061/(ASCE)GT.1943-5606.0001741

21. Lu N, Khorshidi M (2015) Mechanisms for soil-water retention and hysteresis at high suction range. J Geotech Geoenviron 141(8):04015032. https://doi.org/10.1061/(ASCE)GT.1943-5606.0001325

22. Lu N, Likos WJ (2004) Unsaturated soil mechanics. Wiley, New York

23. Monroy R, Zdravkovic L, Ridley A (2010) Evolution of microstructure in compacted London Clay during wetting and loading. Géotechnique 60(2):105–119. https://doi.org/10.1680/geot.8.P.125

24. Musso G, Romero E, Vecchia GD (2013) Double-structure effects on the chemo-hydro-mechanical behaviour of a compacted active clay. Géotechnique 63(3):206–220. https://doi.org/10.1680/geot.SIP13.P.011

25. Nowamooz H, Masrouri F (2010) Relationships between soil fabric and suction cycles in compacted swelling soils. Eng Geol 114(3–4):444–455. https://doi.org/10.1016/j.enggeo.2010.06.005

26. Ohkubo T, Ibaraki M, Tachi Y, Iwadate Y (2016) Pore distribution of water-saturated compacted clay using NMR relaxometry and freezing temperature depression; effects of density and salt concentration. Appl Clay Sci 123:148–155. https://doi.org/10.1016/j.clay.2016.01.014

27. Or D, Tuller M (1999) Liquid retention and interfacial area in variably saturated porous media: upscaling from single-pore to

sample-scale model. Water Resour Res 35(12):3591–3605. https://doi.org/10.1029/1999WR900262

28. Prost R, Koutit T, Benchara A, Huard E (1998) State and location of water adsorbed on clay minerals: consequences of the hydration and swelling shrinkage phenomena. Clay Clay Miner 46(2):117–131. https://doi.org/10.1346/CCMN.1998.0460201

29. Rhaiem H, Tessier D, Pons C, Amara A (1998) Evolution of the microstructure of interstratified Ca-saturated clays during dehydration: SAXS and HRTEM analysis. Clay Miner 33:619–628. https://doi.org/10.1180/claymin.1998.033.4.09

30. Romero E (2013) A microstructural insight into compacted clayey soils and their hydraulic properties. Eng Geol 165:3–19. https://doi.org/10.1016/j.enggeo.2013.05.024

31. Romero E, Simms PH (2008) Microstructure investigation in unsaturated soils: a review with special attention to contribution of mercury intrusion porosimetry and environmental scanning electron microscopy. Geotech Geol Eng 26(6):705–727. https://doi.org/10.1007/s10706-008-9204-5

32. Romero E, Vecchia GD, Jommi C (2011) An insight into the water retention properties of compacted clayey soils. Géotechnique 61(4):313–328. https://doi.org/10.1680/geot.2011.61.4.313

33. Sasanian S, Newson TA (2013) Use of mercury intrusion porosimetry for microstructural investigation of reconstituted clays at high water contents. Eng Geol 158:15–22. https://doi.org/10.1016/j.enggeo.2013.03.002

34. Seiphoori A, Ferrari A, Laloui L (2014) Water retention behavior and microstructural evolution of MX-80 bentonite during wetting and drying cycles. Géotechnique 64(9):721–734. https://doi.org/10.1680/geot.14.P.017

35. Simms PH, Yanful EK (2001) Measurement and estimation of pore shrinkage and pore distribution in a clayey till during soil–water characteristic curve tests. Can Geotech J 38(4):741–754. https://doi.org/10.1139/t01-014

36. Sun WJ, Cui YJ (2017) Investigating the microstructure changes for silty soil during drying. Géotechnique 68(4):370–373. https://doi.org/10.1680/jgeot.16.P.165

37. Tian HH, Wei CF, Lai YM, Chen P (2017) Quantification of water content during freeze–thaw cycles: a nuclear magnetic resonance based method. Vadose Zone J 17:160124. https://doi.org/10.2136/vzj2016.12.0124

38. Todoruk TR, Langford CH, Kantzas A (2003) Pore-scale redistribution of water during wetting of air-dried soils as studied by low-field NMR relaxometry. Environ Sci Technol 37:2707–2713. https://doi.org/10.1021/es025967c

39. Tokunaga TK (2011) Physicochemical controls on adsorbed water film thickness in unsaturated geological media. Water Resour Res 47:W08514. https://doi.org/10.1029/2011WR010676

40. Tuller M, Or D (2005) Water films and scaling of soil characteristic curves at low water contents. Water Resour Res 41:W09403. https://doi.org/10.1029/2005WR004142

41. Vilarrasa V, Rutqvist J, Martin LB, Birkholzer J (2015) Use of a dual-structure constitutive model for predicting the long-term behavior of an expansive clay buffer in a nuclear waste repository. Int J Geomech 16(6):D4015005. https://doi.org/10.1061/(ASCE)GM.1943-5622.0000603

42. Wei X, Hattab M, Fleureau JM, Hu R (2013) Micro-macro-experimental study of two clayey materials on drying paths. B Eng Geol Environ 72(3):495–508. https://doi.org/10.1007/s10064-013-0513-4

43. Yuan SY, Liu XF, Sloan SW, Buzzi OP (2016) Multi-scale characterization of swelling behaviour of compacted Maryland clay. Acta Geotech 11(4):789–804. https://doi.org/10.1007/s11440-016-0457-5

44. Zhang Y, Ye WM, Chen YG, Chen B (2017) Impact of NaCl on drying shrinkage behavior of low-plasticity soil in earthen heritages. Can Geotech J 54(12):1762–1774. https://doi.org/10.1139/cgj-2016-0403

45. Zhang JR, Niu G, Li XC, Sun DA (2020) Hydro-mechanical behavior of expansive soils with different dry densities over a wide suction range. Acta Geotech 15:265–278. https://doi.org/10.1007/s11440-019-00874-y

46. Zhao NF, Ye WM, Chen B, Chen YG, Cui YJ (2019) Modeling of the swelling–shrinkage behavior of expansive clays during wetting–drying cycles. Acta Geotech 14:1325–1335. https://doi.org/10.1007/s11440-018-0718-6